

# GPS determined coseismic slip of the 2021 $M_w$ 7.4 Maduo, China, earthquake and its tectonic implication

Min Wang,<sup>1</sup> Fan Wang,<sup>2</sup> Xin Jiang,<sup>3</sup> Jianbo Tian,<sup>4</sup> Yu Li,<sup>5</sup> Jiaobao Sun<sup>1</sup> and Zheng-Kang Shen<sup>6,7</sup>

<sup>1</sup>State Key Laboratory of Earthquake Dynamics, Institute of Geology, China Earthquake Administration, 100029 Beijing, China

<sup>2</sup>National Geomatics Center of China, 100830 Beijing, China

<sup>3</sup>China Mobile (Shanghai) Information Communication Technology Co., Ltd, 200060 Shanghai, China

<sup>4</sup>Beijing Sixents Technology Co., Ltd, 100094 Beijing, China

<sup>5</sup>China Earthquake Networks Center, 100045 Beijing, China

<sup>6</sup>Department of Geophysics, School of Earth and Space Science, Peking University, 100871 Beijing, China. E-mail: [zshen@ucla.edu](mailto:zshen@ucla.edu)

<sup>7</sup>Department of Earth, Planetary, and Space Sciences, University of California, Los Angeles, Los Angeles, CA 90095-1567, USA

Accepted 2021 November 4. Received 2021 November 4; in original form 2021 June 29

## SUMMARY

The 2021  $M_w$ 7.4 Maduo earthquake occurred on the Jiangcuo fault within the Bayan Har block in eastern Tibet. It is a rather unique event and attests that large earthquakes can occur in the interior of major tectonic blocks within the Tibetan plateau. By processing GPS data observed in the eastern Tibet region, we produce a data set documenting 3-D coseismic displacements of the Maduo earthquake. Using the data set to constrain a coseismic slip model, we find that the earthquake ruptured a nearly vertical fault about 170 km in length, with  $\sim 90\%$  of the moment released in the shallow layer above 20 km depth. The maximum slip of  $\sim 3.6$  m occurred near the surface around a bend in the east segment of the fault. The overall seismic moment release is  $1.82 \times 10^{20}$  N m and is equivalent to  $M_w$ 7.4. Driven by the eastward extrusion of the Tibetan plateau, the deformation field in eastern Tibet is dominated by left-lateral shear, with the strikes of the tectonic faults rotating clockwise from west to east along with the shear stress orientation. This deformation pattern explains the mechanisms of earthquakes along block boundary faults, as well as the ones on faults within the blocks. The Jiangcuo fault is located  $\sim 70$  km south of the East Kunlun fault and could be connected to the Kunlun Mountain Pass fault to its WNW that ruptured during the 2001 Kokoxili earthquake, and a seismic gap of  $\sim 240$  km long between the two faults is worth special attention for its increased earthquake potential.

**Key words:** Space geodetic surveys; Asia; Earthquake dynamics; Earthquake hazards; Seismicity and tectonics.

## 1 INTRODUCTION

The deformation style of the Tibetan plateau has been debated for decades. One school of thought considers that crust is sliced into a limited number of blocks, which are rigid internally and move relative to each other along their boundary faults (e.g. Peltzer & Tapponnier 1988; Avouac & Tapponnier 1993). Another school advocates a viscous sheet model and attributes crustal deformation to be broadly distributed even within blocks (e.g. Royden *et al.* 1997; Flesch *et al.* 2001; England & Molnar 2005). Application of the Global Navigation Satellite System (GNSS) technique to crustal deformation monitoring has provided new observations to aid the debate. For example, Zhang *et al.* (2004) analysed Global Positioning System (GPS) velocities in Tibet and showed that the deformation field is largely continuous. Meade (2007) and Thatcher

(2007), however, interpreted the same data set and found that the rigid block motion model could still hold if the crust was subdivided into a few more smaller blocks than previously envisioned. Further analyses of GPS data with better spatial coverage revealed that deformation within blocks cannot be neglected (e.g. Loveless & Meade 2011; Wang *et al.* 2017a), but its significance relative to deformation along block boundaries is still subject to debate.

Outcome of the debate on crustal deformation style has significant implications on assessment of seismic hazard potential. If the rigid block motion model holds, it suggests that large earthquakes would always occur at block boundaries. Historic and contemporary earthquake catalogues showed that almost all earthquakes of magnitude greater than 8 and 80–90% of earthquakes of magnitude over 7 in China occurred at boundaries of active tectonic blocks, which seems to support this conjecture, at least to some extent (Zhang *et al.*

2003; Zheng *et al.* 2020). Crustal deformation studies so far have mostly concentrated on the block boundary faults or fault zones within Tibet (e.g. Zhang *et al.* 2003; Wang *et al.* 2004, 2017b). However, earthquakes of  $M > 7$ , although rare, can still occur in the interior of major tectonic blocks within the plateau, and one such example is the 1947  $M_{7.7}$  Dari earthquake, which occurred in the interior of the Bayan Har block. The 2021 May 21  $M_w 7.4$  Maduo earthquake provides another proof, as well as an opportunity to study the deformation style and earthquake potential of the Tibetan plateau.

The Bayan Har block is the largest tectonic block in eastern Tibet and is delineated by the East Kunlun fault to the north, the Ganzi–Yushu–Xianshuihe fault to the southwest, and the Longmenshan and Jiuzhaigou–Huya faults to the east (Fig. 1). Seismicity has been active at the block boundaries, with more than a dozen of strong earthquakes occurred in the last half century (Fig. 1). Meanwhile, the block interior is also actively deforming. Questions therefore remain: what is the source of the deformation? Is the strain inside the block elastic and associated with seismic moment accumulation? If so, how will the strain be released, by small-to-moderate-sized earthquakes only, or possibly (although rarely) by large earthquakes as well?

The Maduo earthquake ruptured a section of the Jiangcuo fault (Pan *et al.* 2021; Wang *et al.* 2021), which is located in the interior of the Bayan Har block, and is  $\sim 70$  km south of and in subparallel with the East Kunlun fault (Fig. 1). The earthquake source mechanism has been determined using seismological and geodetic data, which show that the slip was predominantly left lateral. The solutions, however, differ significantly in other parameter estimates, such as fault dip direction and angle, dip slip component, and seismic moment release, etc. (Table 1). In this study, we report a new GPS data set with a dense spatial coverage of the fault rupture region and use that to constrain the fault geometry and slip distribution. Implication of the result for the deformation mechanism of the Bayan Har block within the Tibetan plateau is also discussed.

## 2 GPS DETERMINED COSEISMIC DISPLACEMENTS

The Maduo earthquake occurred at 18:04 (UTC time) on 2021 May 21. We collect GPS data observed from May 18 to May 24 at continuous stations located within  $\sim 300$  km distance from the fault rupture to derive the site coseismic displacements of this event. These continuous stations operated independently by four projects or companies: the national key infrastructure project of the Tectonic and Environmental Observation Network in China (hereinafter referred to as TEONET), the Qinghai Administration of Surveying, Mapping and Geoinformation, the China Mobile (Shanghai) Information Communication Technology Co., Ltd and the Beijing Sixents Technology Co., Ltd. The stations from the latter two companies provide real-time positioning and navigation services, and their GPS antennas are mounted on top of the communication towers. Through data processing and analysis, we validate that qualities of data from most of these stations are not significantly different from those of the crustal deformation monitoring stations, as demonstrated by consistent displacement estimates of more than a dozen closely located station pairs ( $< 3.0$  km in distance). In our final solution, one site in each of the station pairs is retained.

The GPS data processing is carried out using the GAMIT/GLOBK software package (Herring *et al.* 2015, 2018). We first discard the last 6 hr of data observed after the quake on

May 21, and process the remaining data using the GAMIT software to produce one subdaily and six daily solutions. All the sites are loosely constrained, and the daily solutions are combined with those of the TEONET and global IGS network together. We then use the GLOBK software to aggregate the daily combined solutions, rename the stations affected by the quake for their post-event position estimates and tie the solution to the ITRF2008 reference frame by performing a seven-parameter transformation of 50 IGS station positions. In the final solution, station position differences before and after the quake are obtained as the coseismic displacements, and a total of 58 sites with 3-D coseismic displacements are produced (Fig. 2 and Supporting Information Table S1). One note is that the 3-d time-series after the quake at several near-field sites shows notable post-seismic displacements, and the largest displacement accumulated over the 3 d is  $\sim 6$  mm at the site JDUO (Fig. 3). This means that the effect of post-seismic deformation on coseismic displacement estimates is minor, and no more than 3 mm at the near-field sites.

Fig. 2 shows the coseismic displacements associated with the Maduo earthquake, from which it can be seen that the earthquake has produced significant coseismic displacements ( $> 1$  cm) within  $\sim 250$  km distance from the fault rupture. Displacements at the level of millimetres are observed in a larger area. The largest horizontal displacement of  $\sim 0.6$  m is observed at the site QHAJ, which is located  $\sim 15$  km north of the fault rupture and near its east end. The vertical coseismic displacements of  $> 1$  cm are also detected at five sites, with a maximum value of 34 mm at the site QHAK which is located  $\sim 35$  km south of the east end of the fault rupture. Except for a few near-field sites, the overall vertical displacements are small, and the deformation pattern agrees with that caused by left-lateral dislocation across a vertical fault.

## 3 COSEISMIC SLIP MODELLING AND RESULTS

We use SAR data from the Sentinel-1 satellite of the European Space Agency to map the fault trace of the Maduo earthquake (see the Supporting Information for detail). The mapped fault trace is about 170 km long, and can be approximated by four segments with slightly different strike orientations (Supporting Information Fig. S1). We omit a split branch at the east end of the fault (marked by a dashed line in Supporting Information Figs S1 and S2) since slip along this segment is virtually undistinguishable from that of its north neighbouring branch in our coseismic slip model, constrained using GPS data. The averaged strike direction is  $N104^\circ E$ , and the west segment bends  $9^\circ$  southward and the east segment bends  $\sim 17^\circ$  northward respectively. We therefore construct a fault model with four segments accordingly, which all extend to 30 km depth.

We mesh the segments into  $3 \times 3$  km cells, and the relationship between the observed surface displacement array  $d$  and the cell slip parameter array  $s$  is

$$d = \mathbf{G}s + \varepsilon, \quad (1)$$

where  $\mathbf{G}$  is the Green's function matrix of elastic dislocation in a layered media, calculated using the PSGRN/PSCMP code (Wang *et al.* 2006).  $\varepsilon$  is the data error array,  $\varepsilon \sim N(0, D_d)$ , and  $D_d$  is the variance/covariance matrix of the data. The elastic properties of the layered media (Supporting Information Fig. S2) are adopted from regional seismic tomography results of Karplus *et al.* (2011) and Mechie *et al.* (2012).

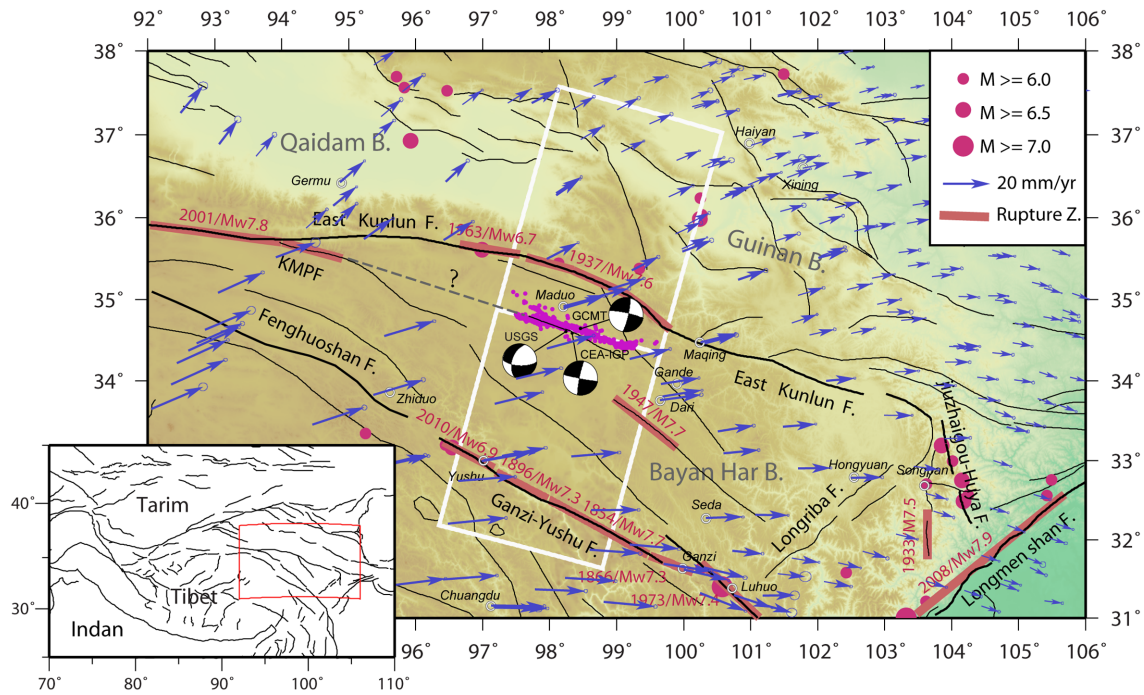


**Figure 1.** Tectonic setting of eastern Tibet. Inset figure outlines the study region in western China. Thin and thick black lines are regional faults and boundary faults of the Bayan Har block, respectively. KMPF: the Kunlun Mountain Pass fault. Rupture zones of historical earthquakes are marked in red (data from Molnar & Deng 1989; Xu *et al.* 2002; Shen *et al.* 2003, 2009; Wen *et al.* 2003; Sun *et al.* 2012). Red dots show earthquakes of  $M \geq 6.0$  from 2019 January 1 to December 31 (<http://earthquake.usgs.gov>). Purple dots represent the aftershocks of the Maduo earthquake (Wang *et al.* 2021). GPS velocities are from Wang & Shen (2020) and referenced to the Eurasia plate.

**Table 1.** Focal mechanism solutions and coseismic slip models of Maduo earthquake.

	Data/solution type	Depth (km)	Strike (°)	Dip (°)	Rake (°)	Moment (Nm)/ $M_w$
	Seismic/ $M_w$	12	282	83	-9	$1.71 \times 10^{20}/7.4$
	Seismic/ $M_w$	23.5	92	67	-40	$1.31 \times 10^{20}/7.3$
	Seismic/ $M_w$	18	281	88	1	$1.90 \times 10^{20}/7.5$
	InSAR/ $M_w$	-	276 <sup>c</sup>	80 <sup>c</sup>	4 <sup>c</sup>	-7.45
	GPS/ $M_w$	-	278	64	-11	$1.85 \times 10^{20}/7.45$
	GPS/ $M_w$	-	284 <sup>c</sup>	87 <sup>c</sup>	6 <sup>c</sup>	$1.82 \times 10^{20}/7.4$

<sup>a</sup><https://www.globalcmt.org/CMTsearch.html>.

<sup>b</sup><https://earthquake.usgs.gov/earthquakes/eventpage/us7000e54r/moment-tensor>.

<sup>c</sup>Numbers are averaged over model.

We employ the least-squares method to solve for the slips and impose a linear (first-order) smoothing and non-negativity constraints on slip components. We minimize the following function:

$$F(s) = (Gs - d)^T D_d^{-1} (Gs - d) + \frac{1}{\beta^2} s^T H^T H s, \quad (2)$$

where  $\mathbf{H}$  is the normal matrix for the first-order smoothing and  $\beta$  is the smoothing factor determined by weighing a trade-off between model resolution and reduced data residual  $\chi^2$ s. Non-negativity constraint ( $s_i \geq 0$ ) is imposed on all the fault cells, and left-lateral slip is considered to be positive for the horizontal component. For the dip component, two separate inversions are performed for the cases of either thrust or down-dip slip, respectively, to determine the preferred slip direction by data fitting.

We test a series of models with different fault dip angles, and for each model, a uniform dip angle is assumed for all the fault segments. The reduced data residual  $\chi^2$ s of these models are plotted in Fig. 4(a), which all suggest a near vertical fault dipping 87° to the north. We also run a series of tests with a range of smoothing factor  $\beta$  for fault slip, and find that varying this factor has no

significant effect on the slip pattern (Supporting Information Fig. S3) and the overall seismic moment release estimate (Supporting Information Fig. S4). The preferred value for  $\beta$  is chosen as 200 mm (Fig. 4b).

The slip distribution of the preferred model is shown in Fig. 5, which illustrates shallow slip for the Maduo earthquake overall, with most of the >1.5 m slip taking place above the 15 km depth. The averaged slip rake angle is  $\sim 6^\circ$ , attesting that the slip is predominantly left lateral. Two peak slip areas with greater than 2.2 and 1.7 m of slip (areas A and B enclosed by grey lines in Fig. 5) are found near the east and west bending sites of the fault, respectively, and the largest slip of  $\sim 3.6$  m is in the east peak slip area near the surface. Because of the small size of fault cells and smoothing over them, the resolutions for most of the individual fault cells are merely 1–2% (Supporting Information Fig. S5). Therefore, a meaningful assessment of the resolution will have to be evaluating averaged slip over multiple fault cells [see Jackson (1979) and Shen *et al.* (1996) for resolution assessment]. Both of the total resolution for the strike-slip component of areas A and B are  $\sim 0.96$ , suggesting that the patterns of high slip areas are well resolved by the data. The



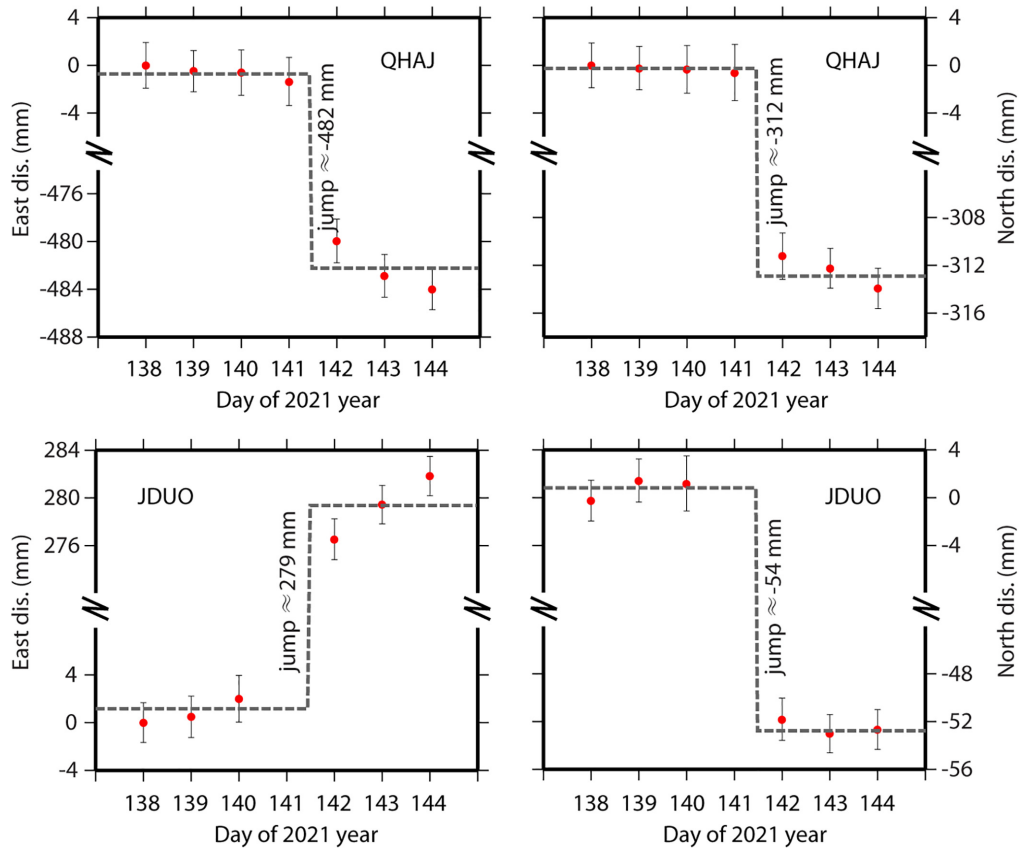


**Figure 3.** GPS horizontal displacement time-series at sites JDUO and QHAJ. QHAJ is located at about 15 km north of the fault rupture and has the largest coseismic displacement, while JDUO is located at about 20 km south of the fault rupture and has the most significant post-seismic displacement, respectively.

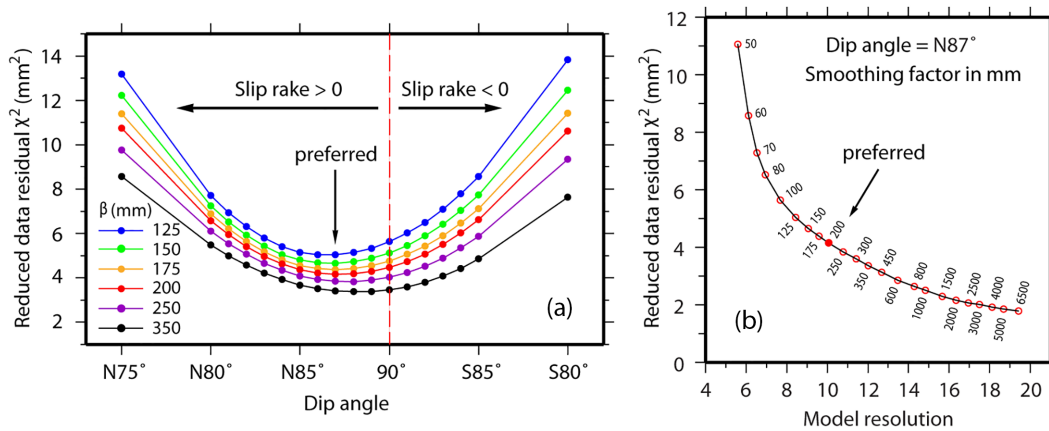


**Figure 4.** (a) The reduced data postfit residual  $\chi^2$ s of models with different fault dip angles. (b) Trade-off curve between model resolution and reduced data postfit residual  $\chi^2$ s.

InSAR data (Hua *et al.* 2021) and partly supported by the geological field survey result (Pan *et al.* 2021). Early geological field surveys found the strike-slip surface displacements of 1–2 m in the areas corresponding to the east and west peak slip areas of our model, and no visible surface rupture trace along a  $\sim 20$  km stretch in the central segment of the fault (Pan *et al.* 2021). However, precise comparison between our model and the geological survey result is difficult, since geological surveys measured only the near-field offsets, while our model depicts integrated offsets over a fault zone

that could be tens to hundreds of metres wide. The spatial pattern of slip distribution suggests that the bending sites on fault could be geometric barriers, which would impede rupture ripping through during small-to-moderate-sized earthquakes and fail only during the larger ones, with which greater seismic moment accumulated during a longer period could be released. This scenario is similar to the rupture history of the Longmenshan fault, whose geometric barriers were ruptured in a cascade mode during the 2008 Wenchuan earthquake (Shen *et al.* 2009; Wan *et al.* 2017).

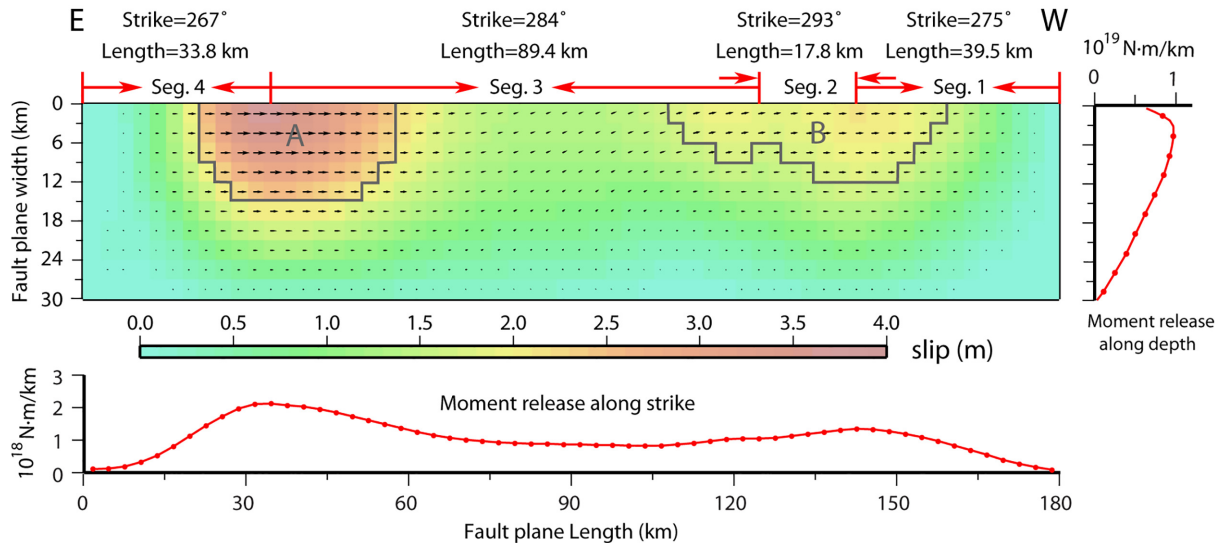


**Figure 5.** Slip distribution for the preferred model. The background colour and small arrows denote the amplitude and direction of the slip, respectively. The bottom and right panels show vertically and laterally integrated seismic moments, respectively. A and B denote two areas with the peak slip.

The Maduo earthquake ruptured the Jianguo fault, which is not part of a known block boundary and was not known to be tectonically active prior to the quake. We project the interseismic GPS velocity data [from Wang & Shen (2020) and shown in Fig. 1] along a profile perpendicular to the Jianguo fault (Fig. 6a). The velocity profile illustrates greater tangential velocity gradient across the East Kunlun and Ganzi–Yushu faults than that in the interior of the Bayan Har block. Previous studies demonstrated that the remaining deformation within the block had to be explained by some sort of distributed internal deformation (e.g. Wang *et al.* 2017b). The broadly distributed deformation also accumulates strain energy on faults within blocks, which will be released eventually by earthquakes. The velocity component normal to the fault does not show significant gradient, indicating that the interseismic deformation field is dominated by left-lateral shear, which is consistent with our coseismic slip model of the Maduo earthquake.

To better understand the tectonic origin of the Maduo earthquake, we plot strain rates interpolated from the regional GPS velocity field in Fig. 6(b). The interpolation is done using the method of Shen *et al.* (2015). Due to the sparse distribution of GPS sites, the strain rate estimates have to be averaged over large areas. However, the result still shows high strain rates in the Bayan Har region, with the amplitudes of the maximum shear strain rate at the level of  $20\text{--}30 \times 10^{-9} \text{ yr}^{-1}$ . The two principal horizontal strain rates are about equal in amplitude and opposite in sign, indicating that deformation is close to simple shear. Note that the direction of the maximum shear strain rate rotates gradually from west to east, from trending E–W at  $\sim 95^\circ$  E to ESE–WNW at  $\sim 102^\circ$  E along the East Kunlun fault, coinciding closely with the changing strike direction of the fault. The direction of the maximum shear strain rate also agrees with other fault strike directions in the region, such as the Jianguo, Dari, Wudaoliang–Changshagongma and Ganzi–Yushu faults (Fig. 6b). We conclude that the deformation field in the Bayan Har region is dominated by lateral shear, which is driven by eastward extrusion of the Tibetan plateau and produces a cluster of wrenching style faults. As the eastward extrusion of the plateau creates clockwise rotation for the crust in east and southeast of the plateau, the direction of the maximum shear strain also rotates clockwise accordingly, together with configuration of the faults manufactured by the stress field.

This explains both the geodetic strain field observed in the region and mechanisms of the earthquakes along major faults such as the East Kunlun and Ganzi–Yushu–Xianshuihe faults, as well as the ones on faults within the blocks such as the Maduo earthquake.

Our model shows that the slip caused by the Maduo earthquake is mainly located above the 15 km depth and with the largest slip near the surface, indicating that the brittle layer ruptured by the earthquake is relatively thin. This inference is consistent with a mechanically weak upper crust, weakened and thinned by hot and easily deforming lower crust, evidenced by high heat flow (Xu *et al.* 2011) and wide presence of low seismic velocity and high electric conductivity zones in the regional lower crust (e.g. Li *et al.* 2014; Zhan *et al.* 2021). The lateral drive of the upper crust facilitates its distributed deformation, and the lower crust may be deforming passively but coherently with the upper crust, and not driving actively as some of the channel flow models envisioned (e.g. Clark & Royden 2000; Cook & Royden 2008).

The Jianguo fault is located at the southern edge of a high strain rate zone across the East Kunlun fault, and could be a southern branch of the fault system (Fig. 6). This fault might be connected to the Kunlun Mountain Pass fault (Pan *et al.* 2021), which is located  $\sim 240$  km WNW of the west tip of the Maduo earthquake surface break and ruptured together with the East Kunlun fault during the 2001  $M_w 7.8$  Kokoxili earthquake (Xu *et al.* 2002). If this is true, the earthquake potential for the unbroken segment between the 2001 and 2021 fault ruptures must have been significantly increased due to the two quakes, and special attention should be paid for its potential hazard.

Previous geodetic studies have shown that the deformation is broadly distributed in Tibet, but it was not clear how that is associated with seismic hazard potential. The historical earthquake record demonstrates that large earthquakes usually occurred on boundary faults of major blocks, and few ever occurred within blocks. For the Bayan Har block, however, we have had two exceptions, the 1947  $M 7.7$  Dari and 2021  $M_w 7.4$  Maduo earthquakes that occurred in the interior of this block. This suggests that active tectonic faults are not only plentiful within the Tibetan plateau blocks, but also capable of producing large earthquakes, although they are not as frequent as the small-to-mediate-sized earthquakes are.

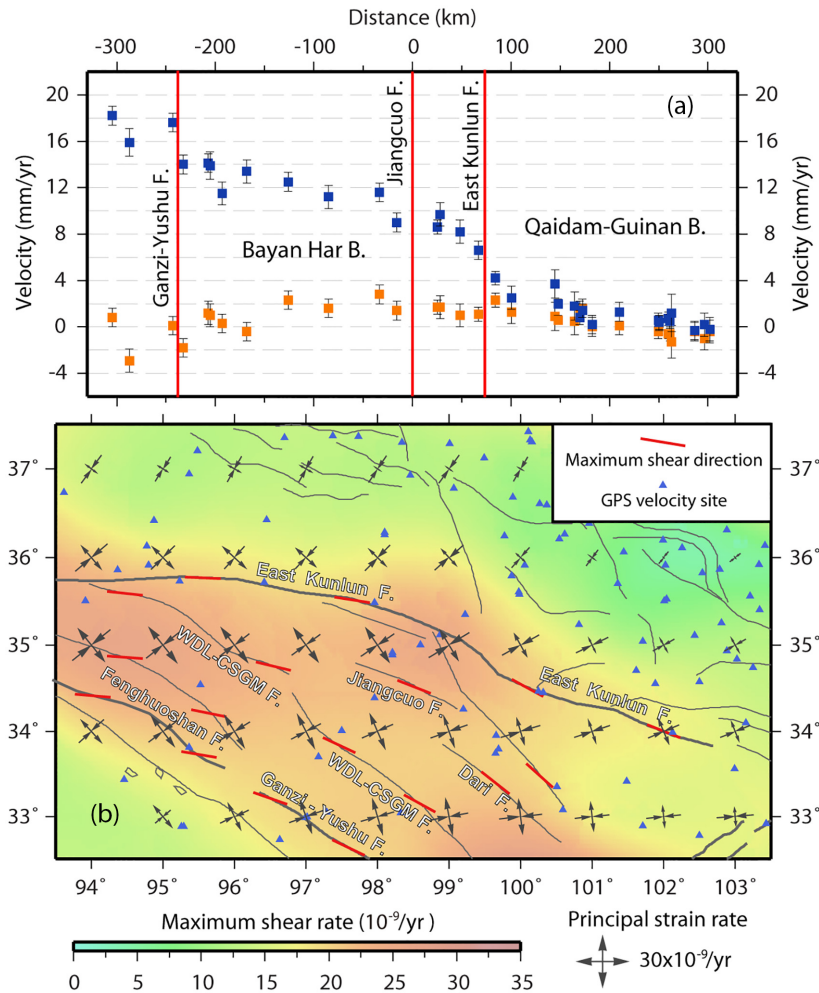


**Figure 6.** (a) GPS velocity profile across Jiangcuo fault, with data from sites enclosed in a white rectangle shown in Fig. 1. Blue and orange squares denote the fault parallel (dextral positive) and normal (extensional positive) components, respectively. Grey error bars represent two standard deviations. (b) Geodetic strain rates interpolated from GPS velocity field. WDL-CSGM F.: the Wudaoliang–Changshagongma fault.

## ACKNOWLEDGEMENTS

We are very grateful to the survey crew who have worked hard to maintain the continuous GNSS networks and retrieve the GPS data that are used in this study. We also appreciate two editors (Jörg Renner and Duncan Agnew) and three reviewers (Kaihua Ding, Romain Jolivet and Eric Hetland) for their detailed and constructive comments. This study is partially supported by research grants from the National Natural Science Foundation of China (41474028 and 41774008).

## DATA AVAILABILITY

The raw GPS data cannot be made available to the public due to state regulation of China. However, the GPS station coseismic displacement data set, slip model of the Maduo earthquake and regional strain-rate data interpolated from GPS velocity field are included in the Supporting Information (Tables S1–S3) for free access.

## REFERENCES

Avouac, J.P. & Tapponnier, P., 1993. Kinematic model of active deformation in central Asia, *Geophys. Res. Lett.*, **20**(10), 895–898.

- Clark, M.K. & Royden, L.H., 2000. Topographic ooze: building the eastern margin of Tibet by lower crustal flow, *Geology*, **28**(8), 703–706.
- Cook, K.L. & Royden, L.H., 2008. The role of crustal strength variations in shaping orogenic plateaus, with application to Tibet, *J. geophys. Res.*, **113**, B08407, doi:10.1029/2007JB005457.
- England, P. & Molnar, P., 2005. Late Quaternary to decadal velocity fields in Asia, *J. geophys. Res.*, **110**, B12401, doi:10.1029/2004JB003541.
- Flesch, L.M., Haines, A.J. & Holt, W.E., 2001. Dynamics of the India–Eurasia collision zone, *J. geophys. Res.*, **106**(B8), 16 435–16 460.
- Herring, T.A., Floyd, M.A., King, R.W. & McClusky, S.C., 2015. *GLOBK Reference Manual, Global Kalman Filter VLBI and GPS Analysis Program, Release 10.6*, Massachusetts Institute of Technology.
- Herring, T.A., King, R.W., Floyd, M.A. & McClusky, S.C., 2018. *GAMIT Reference Manual, GPS Analysis at MIT, Release 10.7*, Massachusetts Institute of Technology.
- Hua, J. et al., 2021. Coseismic deformation field, slip distribution and Coulomb stress disturbance of the 2021  $M_w$ 7.3 Maduo earthquake using Sentinel-1 InSAR observations, *Seismol. Geol.*, **43**(3), 667–691 (in Chinese with English abstract).
- Jackson, D.D., 1979. The use of a priori data to resolve non-uniqueness in linear inversion, *Geophys. J. R. astr. Soc.*, **57**, 137–157.
- Karplus, M.S., Zhao, W., Klemperer, S.L., Wu, Z., Mechie, J., Shi, D., Brown, L.D. & Chen, C., 2011. Injection of Tibetan crust beneath the south Qaidam Basin: evidence from INDEPTH IV wide-angle seismic data, *J. geophys. Res.*, **116**, B07301, doi:10.1029/2010JB007911.

- Li, H., Shen, Y., Huang, Z., Li, X., Gong, M., Shi, D., Sandvol, E. & Li, A., 2014. The distribution of the mid-to-lower crustal low-velocity zone beneath the northeastern Tibetan Plateau revealed from ambient noise tomography, *J. geophys. Res.*, **119**(3), 1954–1970.
- Li, Z., Ding, K., Zhang, P., Wan, Y., Zhao, L. & Chen, J., 2021. Co-seismic deformation and slip distribution of 2021  $M_w$ 7.4 Maduo earthquake from GNSS observation, *Geomatics Inf. Sci. Wuhan Univ.*, doi:10.13203/j.whugis20210301.
- Loveless, J.P. & Meade, B.J., 2011. Partitioning of localized and diffuse deformation in the Tibetan Plateau from joint inversions of geologic and geodetic observations, *Earth planet. Sci. Lett.*, **303**(1–2), 11–24.
- Meade, B.J., 2007. Present-day kinematics at the India–Asia collision zone, *Geology*, **35**(1), 81–84.
- Mechie, J. *et al.*, 2012. Crustal shear ( $S$ ) velocity and Poisson's ratio structure along the INDEPTH IV profile in northeast Tibet as derived from wide-angle seismic data, *Geophys. J. Int.*, **191**(2), 369–384.
- Molnar, P. & Deng, Q., 1989. Faulting associated with large earthquakes and the average rate of deformation in central and eastern Asia, *J. geophys. Res.*, **89**(B7), 6203–6227.
- Pan, J. *et al.*, 2021. Coseismic surface rupture and seismogenic structure of the 2021-05-22 Maduo (Qinghai)  $M_s$ 7.4 earthquake, *Acta Geol. Sin.*, **95**(6), 1655–1670 (in Chinese with English abstract).
- Peltzer, G. & Tapponnier, P., 1988. Formation and evolution of strike-slip faults, rifts, and basins during the India–Asia collision: an experimental approach, *J. geophys. Res.*, **93**(B12), 15085–15117.
- Royden, L.H., Burchfiel, B.C., King, R.W., Wang, E., Chen, Z., Shen, F. & Liu, Y., 1997. Surface deformation and lower crustal flow in eastern Tibet, *Science*, **276**(5313), 788–790.
- Shen, Z.K., Ge, B.X., Jackson, D.D., Potter, D., Cline, M. & Sung, L.Y., 1996. Northridge earthquake rupture models based on the Global Positioning System measurements, *Bull. seism. Soc. Am.*, **86**(1B), S37–S48.
- Shen, Z.-K., Wan, Y., Gan, W., Zeng, Y. & Ren, Q., 2003. Viscoelastic triggering among large earthquakes along the east Kunlun fault system, *Chin. J. Geophys.*, **46**(6), 786–795 (in Chinese with English abstract).
- Shen, Z.-K. *et al.*, 2009. Slip maxima at fault junctions and rupturing of barriers during the 2008 Wenchuan earthquake, *Nat. Geosci.*, **2**, 718–724.
- Shen, Z.-K., Wang, M., Zeng, Y. & Wang, F., 2015. Optimal interpolation of spatially discretized geodetic data, *Bull. seism. Soc. Am.*, **105**(4), 2117–2127.
- Sun, X. *et al.*, 2012. Surface rupture features of the 2010 Yushu earthquake and its tectonic implication, *Chin. J. Geophys.*, **55**(1), 155–170 (in Chinese with English abstract).
- Thatcher, W., 2007. Microplate model for the present-day deformation of Tibet, *J. geophys. Res.*, **112**, B01401, doi:10.1029/2005JB004244.
- Wan, Y., Shen, Z.K., Bürgmann, R., Sun, J. & Wang, M., 2017. Fault geometry and slip distribution of the 2008  $M_w$  7.9 Wenchuan, China earthquake, inferred from GPS and InSAR measurements, *Geophys. J. Int.*, **208**(2), 748–766.
- Wang, H., Zhang, G., Wu, Y. & Ma, H., 2004. The Deformation of active crustal-blocks on the Chinese Mainland and its relation with seismic activity, *Earthq. Res. China*, **18**(1), 54–66.
- Wang, M. & Shen, Z.-K., 2020. Present-day crustal deformation of continental China derived from GPS and its tectonic implications, *J. geophys. Res.*, **125**(2), e2019JB018774, doi:10.1029/2019JB018774.
- Wang, R., Lorenzo-Martín, F. & Roth, F., 2006. PSGRN/PSCMP—a new code for calculating co- and post-seismic deformation, geoid and gravity changes based on the viscoelastic-gravitational dislocation theory, *Comput. Geosci.*, **32**(4), 527–541.
- Wang, W., Qiao, X., Yang, S. & Wang, D., 2017a. Present-day velocity field and block kinematics of Tibetan Plateau from GPS measurements, *Geophys. J. Int.*, **208**(2), 1088–1102.
- Wang, W., Fang, L., Wu, J., Tu, H., Chen, L., Lai, G. & Zhang, L., 2021. Aftershock sequence relocation of the 2021  $M_s$ 7.4 Maduo earthquake, Qinghai, China, *Sci. China D*, **64**(8), 1371–1380.
- Wang, Y., Wang, M. & Shen, Z.-K., 2017b. Block-like versus distributed crustal deformation around the northeastern Tibetan plateau, *J. Asian Earth Sci.*, **140**, 31–47.
- Wen, X., Xu, X., Zheng, R., Xie, Y. & Wan, C., 2003. Average slip-rate and recent large earthquake ruptures along the Garzê–Yushu fault, *Sci. China D*, **46**, 276–288.
- Xu, M., Zhu, C., Rao, S. & Hu, S., 2011. Difference of thermal structure between eastern edge of Tibet Plateau and western Sichuan Basin, *Chin. J. Geol.*, **46**(1), 203–212 (in Chinese with English abstract).
- Xu, X., Chen, W., Ma, W., Yu, G. & Chen, G., 2002. Surface rupture of the Kunlun earthquake ( $M_s$ 8.1), northern Tibetan Plateau, China, *Seismol. Res. Lett.*, **73**(6), 884–892.
- Zhan, Y. *et al.*, 2021. Deep structure and seismogenic pattern of the 2021.5.22 Madoi (Qinghai)  $M_s$ 7.4 earthquake, *Chin. J. Geophys.*, **64**(7), 2232–2252 (in Chinese with English abstract).
- Zhang, P.-Z., Deng, Q., Zhang, G., Ma, J., Gan, W., Min, W., Mao, F. & Wang, Q., 2003. Active tectonic blocks and strong earthquakes in the continent of China, *Sci. China D*, **46**, 13–14.
- Zhang, P.-Z., Shen, Z.-K., Wang, M., Gan, W., Bürgmann, R. & Molnar, P., 2004. Continuous deformation of the Tibetan Plateau from global positioning system data, *Geology*, **32**(9), 809–812.
- Zhang, Z. & Xu, L., 2021. The centroid moment tensor solution of the 2021  $M_w$ 7.5 Maduo Qinghai earthquake, *Acta Seismol. Sin.*, **43**(3), 387–391 (in Chinese).
- Zheng, W., Wang, Q., Yuan, D., Zhang, D., Zhang, Z. & Zhang, Y., 2020. The concept, review and new insights of the active-tectonic block hypothesis, *Seismol. Geol.*, **42**(2), 245–270 (in Chinese with English abstract).

## SUPPORTING INFORMATION

Supplementary data are available at [GJI](https://doi.org/10.1002/eqe20210301) online.

**Maduo\_Eq\_supp\_rev2.docx**

**Table\_supp.zip**

**Figure S1.** Fault surface trace of the Maduo earthquake, depicted by the range offset data in the line-of-sight directions from SAR ascending (a) and descending (b) track data. Solid lines are segments adopted for the coseismic slip model, and a dashed line marks a subsegment at the east end of the fault, which is omitted in the model.

**Figure S2.** Earth structure model in depth. Left: seismic velocity profile. Right: density profile.

**Figure S3.** Fault slip distribution with smoothing factor  $\beta = 350$  mm (dip angle =  $N87^\circ$ ).

**Figure S4.** Seismic moment release estimate versus model smoothing factor.

**Figure S5.** Slip resolution distribution for the preferred model.

**Figure S6.** Slip distribution of test model with two GPS sites close to the slip peaks removed from data input. The maximum slip of the solution is reduced from 3.6 to 2.9 m, but the overall pattern and locations of the peak slips are unchanged.

Please note: Oxford University Press is not responsible for the content or functionality of any supporting materials supplied by the authors. Any queries (other than missing material) should be directed to the corresponding author for the paper.